Heritage Science

RESEARCH

Open Access

Microbial corrosion on underwater pottery relics with typical biological condensation disease

Meng Zhao[1], Yang Zhai[2*], Jing Zhao[1*], Wenhui Zhou[3], Luo Zhao[4], Yan Ge[4], Kexin Zhang[1] and Hongjie Luo[1]

Abstract

Underwater pottery relics salvaged from shipwrecks are vulnerable to physical, chemical and biological corrosion. In this study, the microscopic morphology and structural composition of glazed pottery fragments excavated from the South China Sea as well as purple clay teapot samples from the Yangtze River Estuary II shipwreck were analyzed by means of optical microscopy, scanning electron microscope equipped with energy dispersive spectrometer, X-ray diffraction, X-ray photoelectron spectroscopy, Fourier infrared transform spectroscopy and photoluminescence spectroscopy. According to the research results, the corrosion products deposited on the surface of the glazed pottery fragment from the South China Sea mainly included FeOOH and MnO_2, whereas those on the surface of the purple clay teapot fragment from the Yangtze River Estuary II shipwreck primarily incorporated FeS_2 and FeS. According to the corrosion phenomenon, it was speculated that the underwater pottery relics were mainly corroded by different microorganisms in the underwater environment, including manganese-oxidizing bacteria, dissimilatory metal-reducing bacteria and sulfate-reducing bacteria. As the corrosion process of these cultural artifacts was described and related models were established, this study provides valuable reference for the disease removal and protection of pottery relics.

Keywords Underwater pottery relics, Bacteria, Biomineralization, Corrosion mechanism

Introduction

Natural processes regulate the development and evolution of the shipwreck sites, whose formation is a complex course involving various physical, chemical, and biological phenomena [1]. Part of the underwater pottery relics were attached to underwater organisms before they were salvaged, and engaged in the recirculation of nutrients of the ocean, playing a vital role in the underwater ecosystem, and constituting the bottom layer for the colonization of underwater organisms and the development of stable communities over time [2, 3].

During the Song Dynasty, the southeast coast of China with Fujian as the center emerged as an important hub for constructing the Maritime Silk Road of China's world maritime economic, trade, transportation and cultural exchanges. The Fujian maritime space located along the ancient maritime Silk Road of China, was potentially home to a large amount of underwater cultural relics. Since 2005, numerous underwater cultural relics dating back the late Tang Dynasty to the Qing Dynasty, have been discovered in Fujian maritime space. At present, the excavated underwater cultural relics were dominated by pottery [4], and plenty of bryozoans and some shellfish

*Correspondence:
Yang Zhai
zhaiyang73@163.com
Jing Zhao
zhaojing@mail.sic.ac.cn
[1] Shanghai Institute of Ceramics, Chinese Academy of Sciences, Shanghai 200050, China
[2] Shanghai Museum, Shanghai 200003, China
[3] Institute of Cultural Relics and Archeology, Fujian Museum, Fuzhou 350025, China
[4] Shanghai Cultural Heritage Conservation and Research Centre, Shanghai 200031, China

deposits were found on the surface of the glazed pottery samples. Bryozoans are a group of fixed living moss animals that prefer to live in clean, algae rich, and dissolved oxygen rich waters. Bryozoans adapt to temperatures in various regions and are widely distributed around the world. Freshwater bryozoans grow vigorously in spring and autumn (water temperature of 25–28 ℃). Bryozoans belong to a type of large biological fouling in water bodies that utilize the energy of water movement to carry away waste and obtain food [5, 6]. In November 2022, the shipwreck named Yangtze River Estuary II of Tongzhi Period of Qing Dynasty (AD 1862–1875) was salvaged from the Yangtze River Estuary in Shanghai, which was one of the most intact ancient wooden shipwrecks in China, with a huge number of cultural relics, such as exquisite porcelain and purple clay pottery [7]. The Yangtze River Estuary II shipwreck was about 38.1 m long and 9.9 m in width, located in the Yangtze River Estuary at a depth of 8–10 m and was buried in 5.5 m of mud with 31 compartments [8]. Different from findings in the Fujian maritime space, plenty of oysters were bound on the surface of the purple clay teapot fragment samples. Due to long lasting exposure to underwater conditions, proteins, polysaccharides, bacteria and other underwater organisms inevitably embedded on the surface of such materials, which further led to reduced service life and microbial corrosion of the materials [9]. Furthermore, shells of underwater organisms attached to the surface of cultural relics would remain in situ after natural death or death due to environmental changes, forming a thick layer of biological condensation. Currently, archaeological excavation revealed that such underwater organisms attached to the cultural relics include bivalve molluscs with a hard shell such as oysters, crustaceans such as barnacles, moss animals such as bryozoans, as well as coelenterates such as corals, etc. [10–12]. Benthos or fouling organisms serve as the main types of organisms that affect the formation of condensation on the surface of cultural relics. As the colonization of some benthos is affected by the properties of the matrix, the roughness of the matrix is a part of the influencing factors [13]. In addition, the composition and content of the substances in the biological condensation are related to microorganisms. In the ocean, all natural and artificial substrates are covered with biofilms composed mainly of microorganisms [14], whose composition and age may affect the attachment of underwater organisms [15, 16]. Previous studies have shown that microorganisms and their metabolites can attach to the metal surface and accelerate or inhibit the corrosion process, while microbial corrosion always depends on the formation of biofilm on the eroded surface [17–19]. At present, the research regarding biological condensation on the surface of the excavated underwater cultural relics mainly focuses on the composition structure, microscopic morphology of the condensation, as well as the materials and technologies for removing the condensation, etc. However, relatively few studies have been conducted on the microbial corrosion and biomineralization at the interface between the condensation and cultural relics [11, 20, 21].

In order to analyze the corrosion of biological condensation on the surface of pottery artifacts in different sea areas, both the glazed pottery fragment salvaged from the South China Sea and the purple clay teapot fragment from the Yangtze River Estuary II shipwreck were analyzed by optical microscope (OM) analysis, scanning electron microscope equipped with energy dispersive spectrometer (SEM-EDS) analysis, X-ray diffraction (XRD) analysis, X-ray photoelectron spectroscopy (XPS) analysis, Fourier transform infrared spectroscopy (FTIR) analysis and photoluminescence spectroscopy (PL) analysis in this study, and corresponding analysis were made. The contributing factors for the formation of condensation and the influence of microbial corrosion on the surface of underwater pottery relics were determined, along with the explanation of corrosion process and the establishment of the related corrosion model.

Materials and methods

Materials

Fragment of the glazed pottery salvaged from the South China Sea and that of the purple clay teapots from the Yangtze River Estuary II shipwreck were selected, numbered NH-1 and CJK-1 respectively. As shown in Fig. 1b, a great amount of bryozoans and certain shellfishes were attached to the surface of the glazed pottery, and after the natural removal of these organisms, brownish-yellow residual substance could be displayed. What is more, underwater organisms such as oysters were also attached to the surface of the matrix of the purple clay teapot fragment salvaged from the Yangtze River Estuary, and there was a residual black substance after elimination of such attachments, as shown in the red box in Fig. 2b.

Methods

OM analysis

An optical microscope XTZ-4KHD from Shanghai Optical Instrument Factory (China) was used to observe the microscopic morphology of the surface of the attachment, the surface of the specimen and the cross section, and the observation was made at 0.7 and 3.5 magnifications.

SEM-EDS analysis

A field-emission scanning electron microscope Verios G4 from FEI Company (America) equipped with an energy

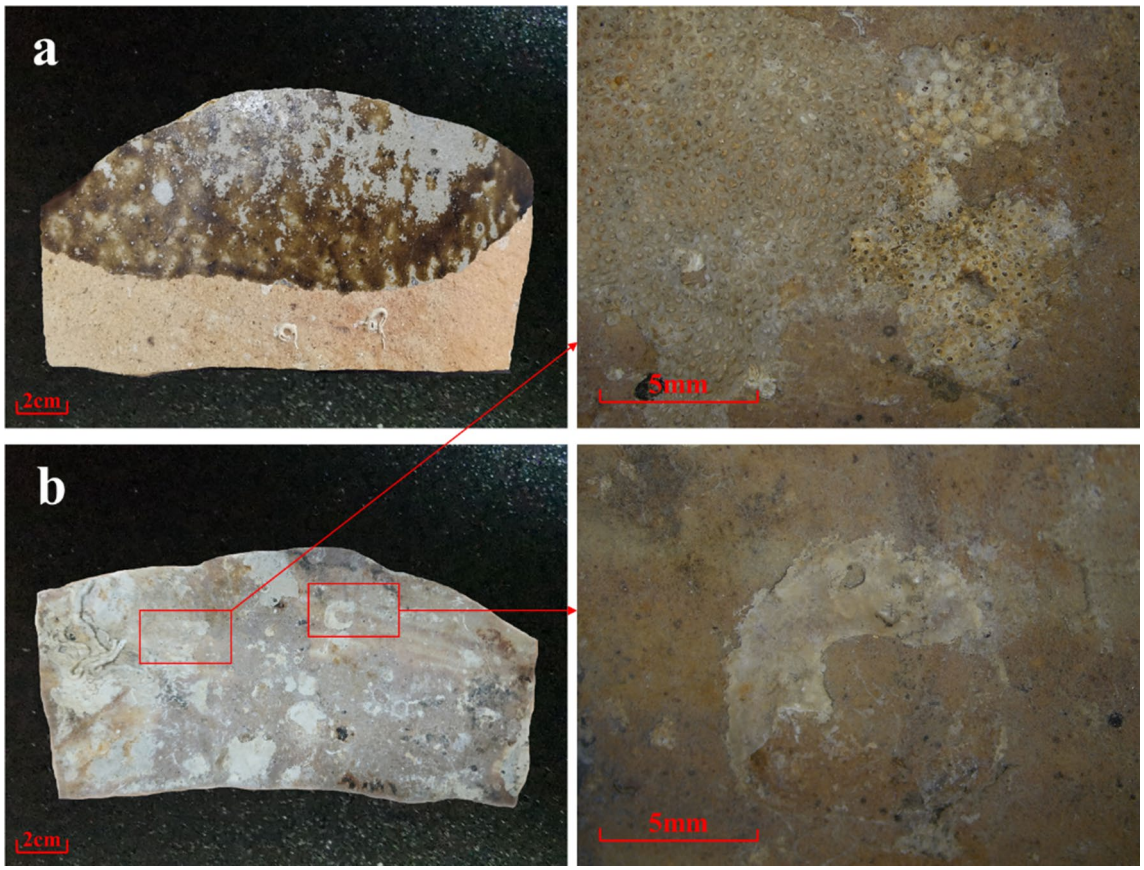

Fig. 1 **a** Glaze surface of NH-1. **b** The attachments on the surface of matrix

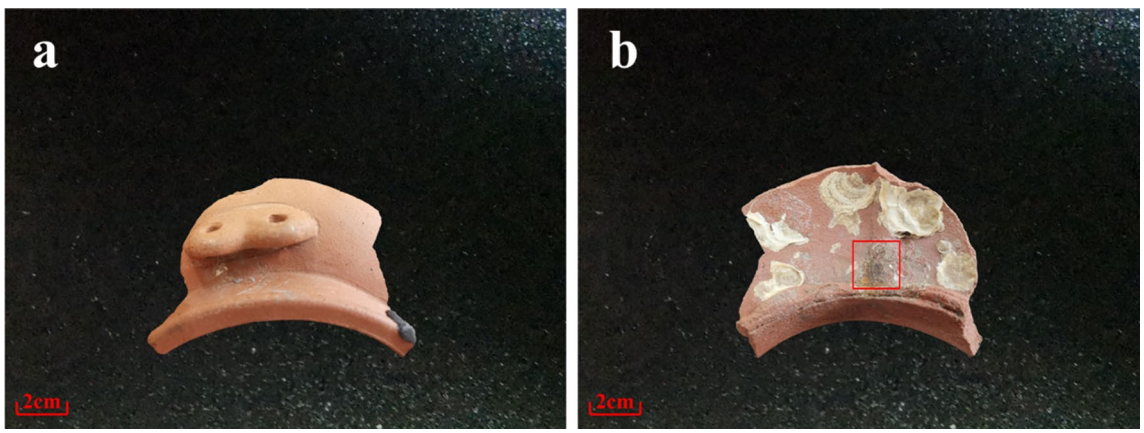

Fig. 2 **a** Pure surface of CJK-1. **b** The attachments on the surface of matrix

dispersive spectrometer was used to analyze the microscopic morphology and element distribution of the sample after 3 nm platinum plating. The set voltage was 10 kV, and the working distance varied from 3.9 to 5.3 mm. The test results included secondary and backscattered electron images.

XRD analysis

A micro focal spot two-dimensional (2D) X-ray diffractometer D8 Discover from Bruker (Germany) was used to examine the sample corrosion area. The maximum voltage of the instrument was 60 kV, the maximum tube current was 80 mA, the optical tube power was 2.2 kW

(Cu target), and the angle reproducibility was ± 0.0001°. A Vantec 500 2D surface detector with a test spot diameter of 0.5 mm and an integration time of 300s was used.

XPS analysis

An X-ray photoelectron spectroscopy ESCAlab250 from Thermo Fisher Scientific (America) was used to examine the valence states of different elements in the corroded region of a sample. The excitation light source was Al K_{α}X-ray, the power was 15 kW, the beam spot size was 500 μm, and the base vacuum of the analysis chamber was 8×10^{-8} Pa. The photoelectron spectra for analysis were recorded at a flux energy of 20 eV, residence time of 50 ms, and step size of 0.05 eV.

FTIR analysis

A Fourier transform infrared spectrometer Spotlight 400 from Perkin Elmer (America) was used to test the organic molecular structure of corrosive substances. The spectral detection range was 500–4000 cm^{-1}, the spectral resolution was 16 cm^{-1}, and the wave number accuracy was better than 0.008 cm^{-1}.

PL analysis

The steady state measurement mode of steady state and transient fluorescence spectrometer FLS 920 from Edinburgh Instruments (Britain) was used to examine the corrosion area on the sample surface. The steady state measurement mode uses the 450 W xenon lamp and the nanosecond and microsecond pulsed flash lamp as the excitation light source, and the voltage and current of the xenon lamp are 17 V and 25 A after the power supply is stabilized. Under the test condition of excitation wavelength 222 nm and slit 2 nm and the test condition of excitation wavelength 220 nm and slit 6 nm, respectively, the emission spectra of the samples in the range of 250 to 700 nm were measured.

Results and discussion

Morphology and composition analysis of the surface of underwater pottery relics and their biological condensation attached on the surfaces

Glazed pottery fragment salvaged from the South China Sea and its biological condensation attached on the surface

Plenty of bryozoans were attached to the surface of sample NH-1. OM was used to observe the macroscopic morphological characteristics of the surface of the bryozoans (Fig. 3a), the adhesion surface of the bryozoans in contact with the glazed pottery matrix (Fig. 3b), the surface of the glazed pottery matrix after disposal of the bryozoans (Fig. 3c) and the cross section of the glazed pottery matrix (Fig. 3d). It was observed that the surface of the bryozoans was filled with hollow calcareous bones, and a great deal of particles of the glazed pottery matrix were bound to the adhesion surface between the bryozoans and the glazed pottery matrix. Meanwhile, the surface of the glazed pottery matrix after the shedding of the bryozoan presented

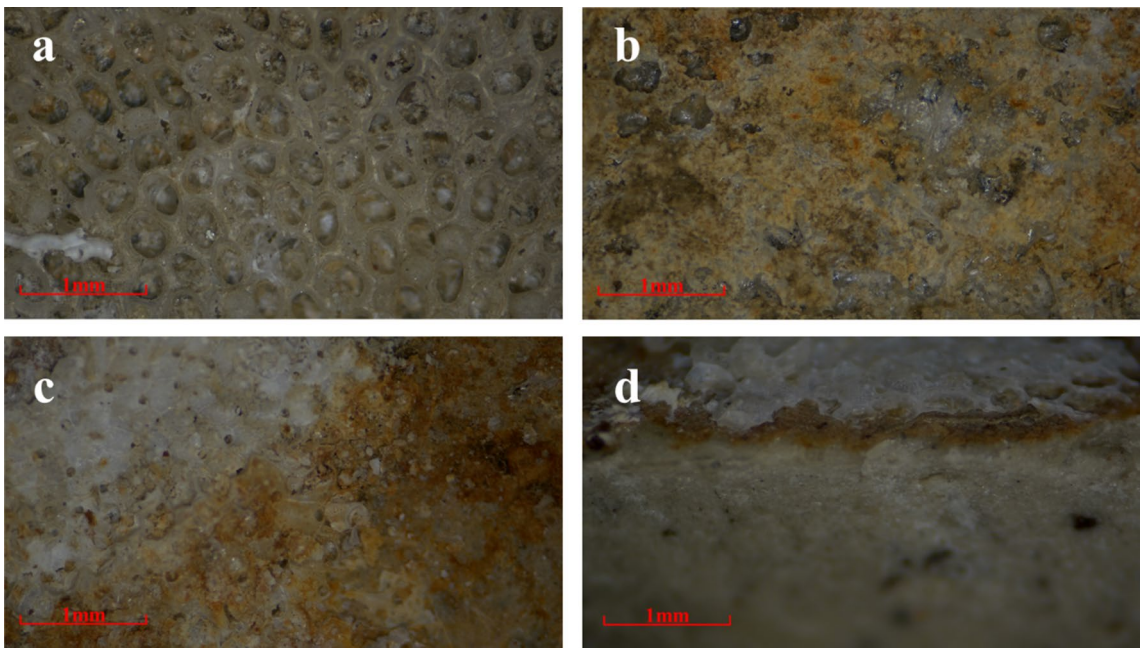

Fig. 3 Optical morphologies of NH-1. **a** The surface of bryozoans. **b** The adhesion surface of the bryozoans in contact with the glazed pottery. **c** The surface of the glazed pottery after the shedding of the bryozoans. **d** The cross section of the glazed pottery

pits in certain regions, and the contact between the glazed pottery matrix and the bryozoans was obviously loose.

SEM-EDS was used to test the micromorphology and element distribution on the surface of the bryozoans, the adhesion surface of the bryozoans in contact with the surface of NH-1, the surface of NH-1 after the shedding of the bryozoans, the surface of the shellfish bonded to the NH-1 surface, the surface of NH-1 after shell shedding and the cross section of NH-1. Figure 4 showed the morphology of the surface of bryozoans. Apart from calcareous sediments, short rod-shaped microbial colonies with main element C also existed.

Figure 5 showed the morphology of the adhesion surface of the bryozoans in contact with NH-1 surface. EDS results of Fig. 5b showed that there was a pleated membrane material with a C element content of 87.01% on the bryozoans adhesion surface (Table 1), and the pleated protrusions of the membrane material were in point contact with the pottery sample.

As demonstrated in Fig. 6, when the bryozoans were removed in a natural way, pottery particles in certain areas on the glazed pottery matrix surface were brownish-yellow and porous (Fig. 6a), with the existence of biofilm (Fig. 6b). The EDS results in Fig. 6a showed that in addition to Al and Si elements, which accounted for 5.02% and 8.50% respectively, there were 9.64% and 18.08% of Mn and Fe on the surface of the matrix (Table 1).

In addition to a large area of bryozoan symbionts, shellfish deposits also existed on the surface of the glazed pottery, as shown in Fig. 7. The area with the greatest bonding force with the pottery matrix was in the shape of a vortex (Fig. 7a), with the banded contact surface mainly consisting of C element (Fig. 7b), and some areas bonded to pottery particles (Fig. 7c; Table 2).

After the natural shedding of the shellfish (Fig. 8), it was observed that membranous cement with C element content of 33.11% existed on the surface of the glazed pottery matrix (Fig. 8e), along with lamellar distribution with high Fe content in local areas (Fig. 8c; Table 3).

Similar to the surface changes, the cross section of NH-1 in Fig. 9 was covered with obvious membranous cement. In certain areas, clear microbial flora mainly composed of C element can be observed (Fig. 9c), as well as high content of Na and Cl elements on the surface. Additionally, there was a lamellae with high content of Fe in the corrosion pits (Fig. 9d–f), which was presumed to be the state of the formation of the iron-bearing lamellae in Fig. 8c (Table 4, Figs. 10, 11).

The white shell deposited on the surface of NH-1 tested by XRD analysis turned out to be mainly $CaCO_3$ and (Ca, Mg)CO_3 (Fig. 12a), whereas the major corrosion products in the brownish-yellow corrosion region after bryozoans shedding were FeOOH and MnO_2 (Fig. 12b). In order to further identify the corrosion products generated on the surface of NH-1, XPS was used to test the ion valence states of Fe and Mn in the brownish-yellow corrosion region. As set forth in Fig. 13a, the spectrum of Fe 2p showed two peaks with binding energy values of 711.08 eV and 725.3 eV, which can be assigned to Fe $2p_{1/2}$ and Fe $2p_{3/2}$ respectively. The binding energy values of Fe $2p_{3/2}$ conformed to the valence range of Fe^{3+}, which was consistent with the valence state of Fe in the structure of FeOOH. As illustrated in Fig. 13b, the spectrum of Mn 2p showed two peaks with binding energy values of 641.31 eV and 651.4 eV, which can be assigned to Mn $2p_{1/2}$ and Mn $2p_{3/2}$ respectively, and the binding energy

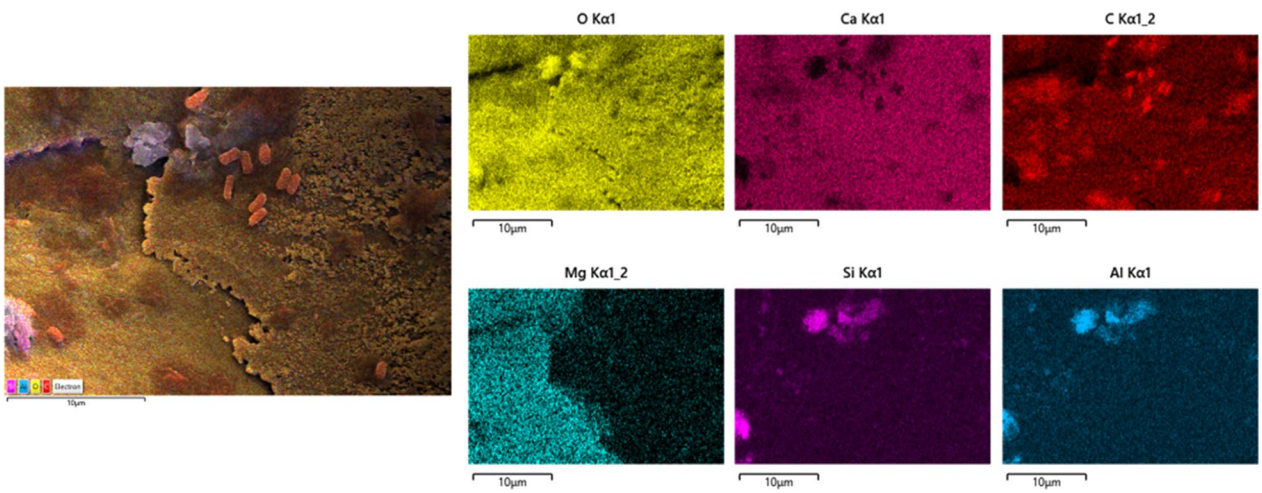

Fig. 4 SEM micromorphology and element distribution of the surface of bryozoans

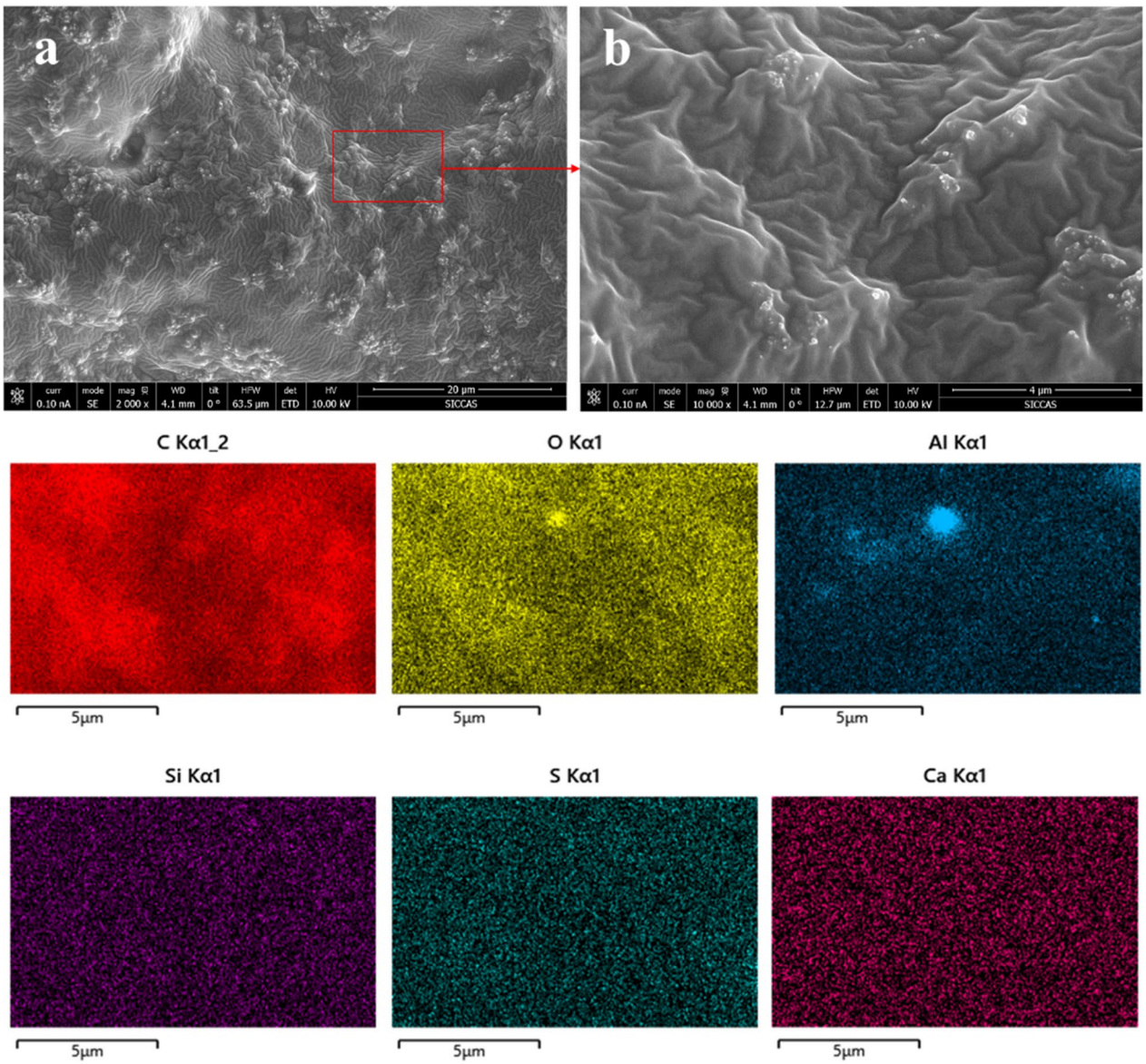

Fig. 5 SEM microscopic morphology and element distribution of the bryozoan adhesion surface in contact with NH-1 surface

value of Mn $2p_{3/2}$ matches Mn^{4+}, which was consistent with the valence state of Mn in the structure of MnO_2. The analytical characterization of Fe and Mn by XPS analysis corresponded to the test results of XRD.

Purple clay teapot fragment from the salvaged Yangtze Estuary II shipwreck and its biological condensation on the surface

The surface of the purple clay teapot fragment sample CJK-1 from the Yangtze River Estuary were covered with oysters. To be more specific, the outermost layer of oysters in Fig. 14a was distributed in lamellar form, with Ca and C elements of 50.52% and 8.14%, respectively (Table 5), and there was a membranous cement on the surface (Fig. 14b). The surface of oysters in contact with CJK-1 also presented membranous cement (Fig. 15a), accompanied by flower-cluster substance with high contents of Fe, S, C and O elements (Fig. 15b; Table 6).

The surface morphology of CJK-1 in contact with oysters in Fig. 16 was similar to that of Fig. 15, which presented flower-cluster substance with high contents of Fe and S (Fig. 16a), and acicular, flakelike and spherical attachments containing Al and Si elements covered by membranous cement (Fig. 16b, c; Table 6).

The crystalline phase structure of the black corrosion region after oysters shedding on the surface of CJK-1 was

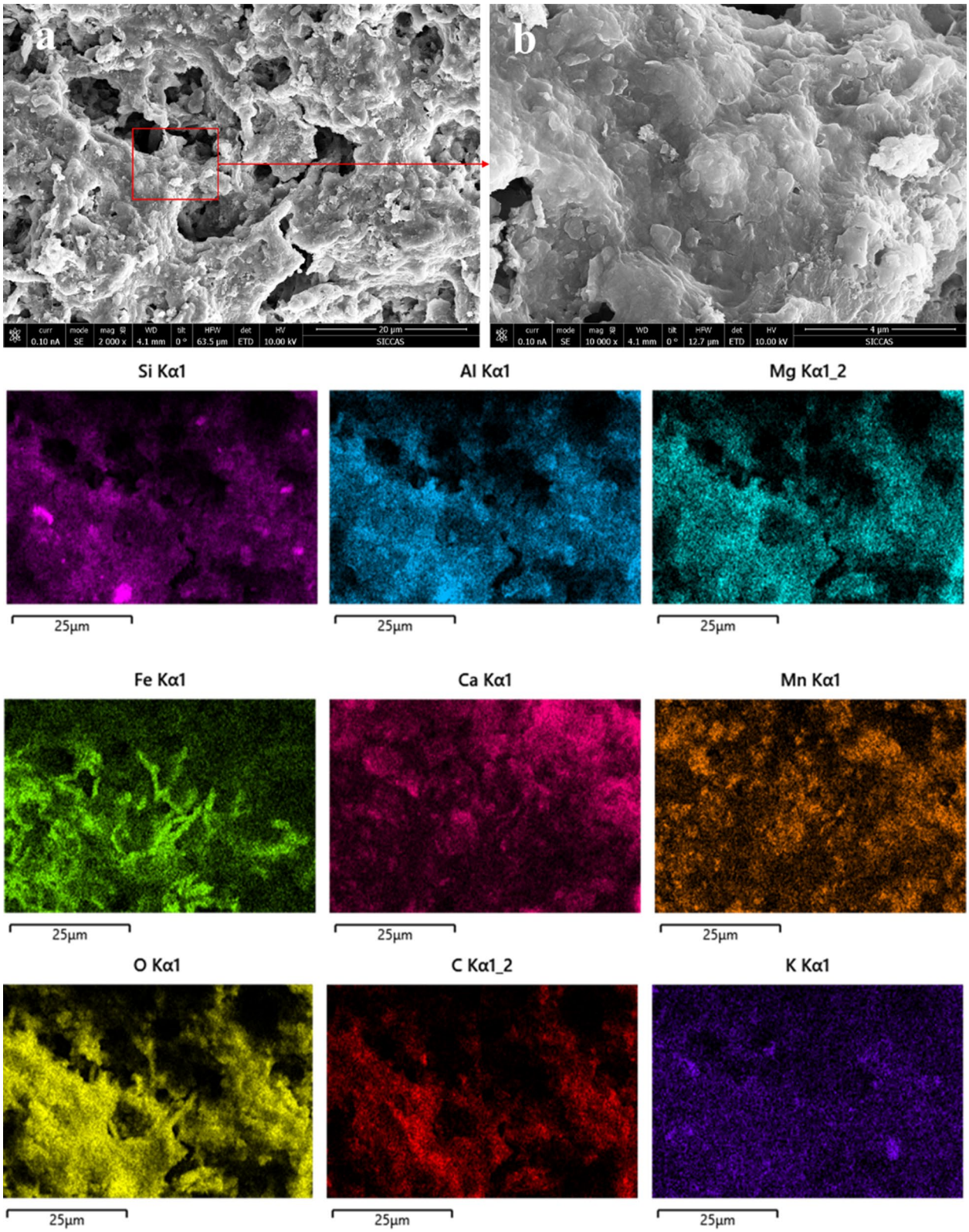

Fig. 6 SEM micromorphology and element distribution on the surface of NH-1 after the shedding of the bryozoans

Table 1 Element contents on the bryozoan adhesion surface in contact with NH-1 surface (Fig. 5b) and on the surface of NH-1 after the shedding of the bryozoans (Fig. 6a) (wt%)

	C	O	Mg	Al	Si	K	Ca	Fe	Mn	S
Figure 5b mapping	87.01	11.82	–	0.34	0.11	–	0.31	–	–	0.41
Figure 6a mapping	8.15	36.89	2.52	5.02	8.50	0.97	10.23	18.18	9.64	–

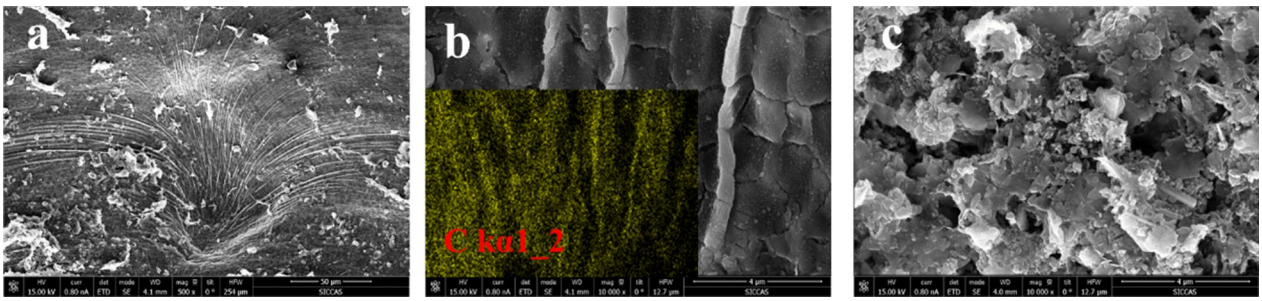

Fig. 7 SEM micromorphology. **a** The adhesion surface in the shape of a vortex. **b** The banded adhesion surface. **c** The adhesion pottery particles surface. **d** The shellfish bonded to the NH-1 surface

Table 2 Element contents in different regions of shellfish adhesion surface in contact with NH-1 surface (wt%)

	C	O	Na	Mg	Al	Si	Ca	Fe	S
Figure 7b mapping	11.20	46.76	0.28	1.59	0.27	0.63	38.27	0.33	0.67
Figure 7c mapping	9.28	45.62	0.46	1.14	1.72	2.27	37.48	2.04	–

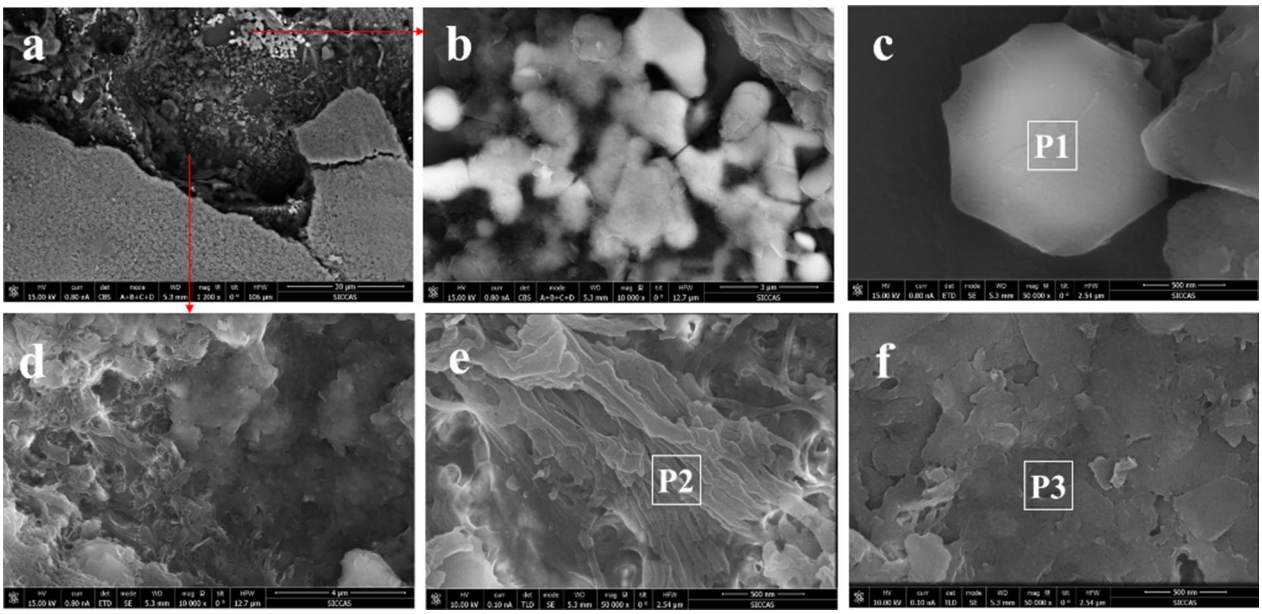

Fig. 8 SEM morphology after shellfish shedding. **a** Pitting. **b**, **c** Fe-containing lamellar region. **d**–**f** Membranous cement (**d**–**f**) on the surface of NH-1

Table 3 Elements contents in different areas of NH-1 surface of glazed pottery after shellfish shedding (wt%)

	C	O	Na	Mg	Al	Si	K	Ca	Ti	Fe	Mn
P1	3.23	3.78	–	0.24	2.47	3.53	0.75	1.13	2.50	81.51	0.87
P2	33.11	33.13	0.35	0.30	6.37	19.89	2.96	2.17	0.35	1.37	–
P3	9.04	41.09	0.42	0.65	14.24	26.51	3.41	1.05	0.34	3.60	–

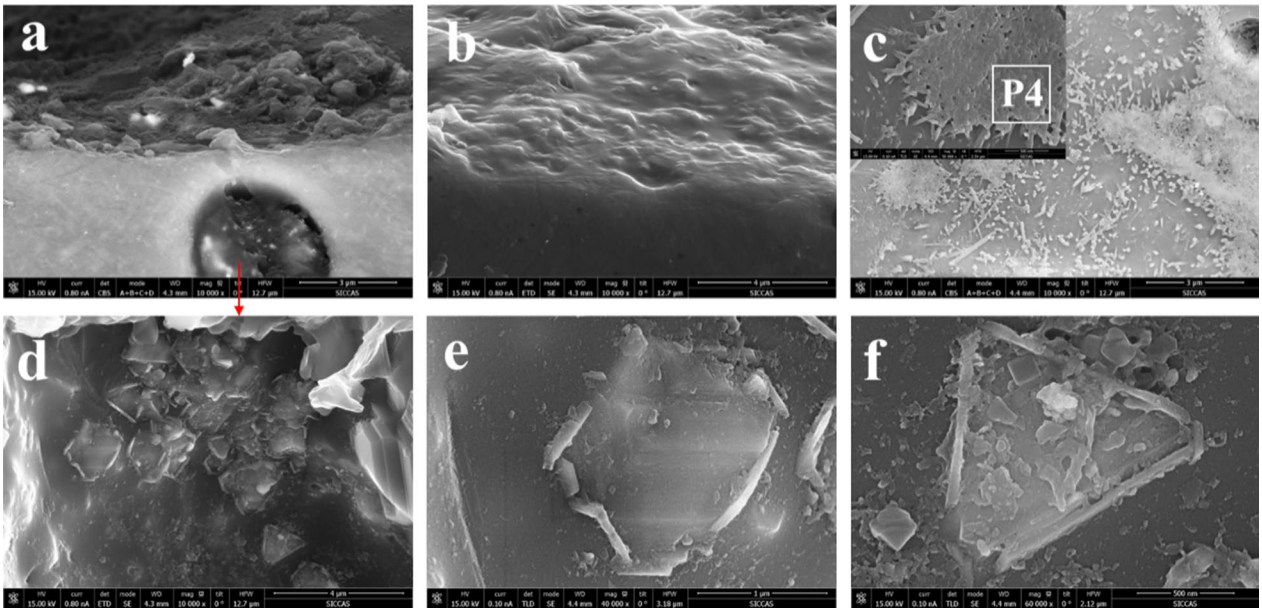

Fig. 9 SEM morphology in the cross section of NH-1. **a** Corrosion pits. **b** Membranous cement. **c** Microbial flora. **d**–**f** Fe-containing lamellae

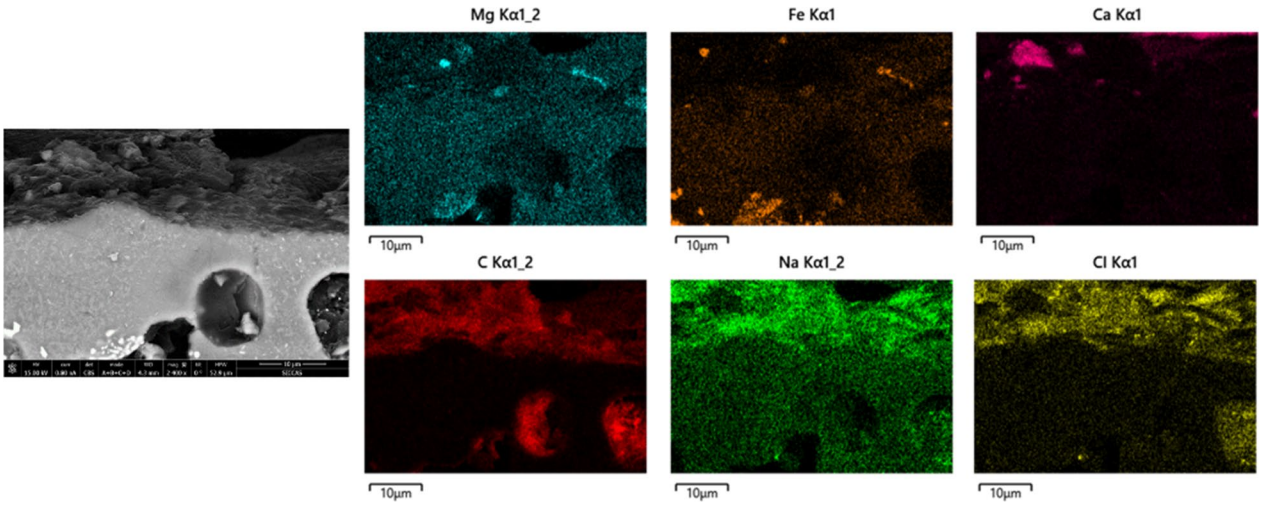

Fig. 10 SEM morphology and element distribution of corrosion pits in cross section of NH-1

tested by XRD, and the test results revealed that the products in this region were mainly FeS_2 and FeS (Fig. 17). Furthermore, XPS was used to test the valence of Fe and S in the black corrosion region after oysters shedding on the surface of CJK-1. As shown in Fig. 18a, the spectrum of Fe 2p shows two peaks with binding energy values of 711.87 eV and 725.6 eV, which can be assigned to Fe $2p_{1/2}$ and Fe $2p_{3/2}$, respectively. The binding energy of Fe $2p_{3/2}$

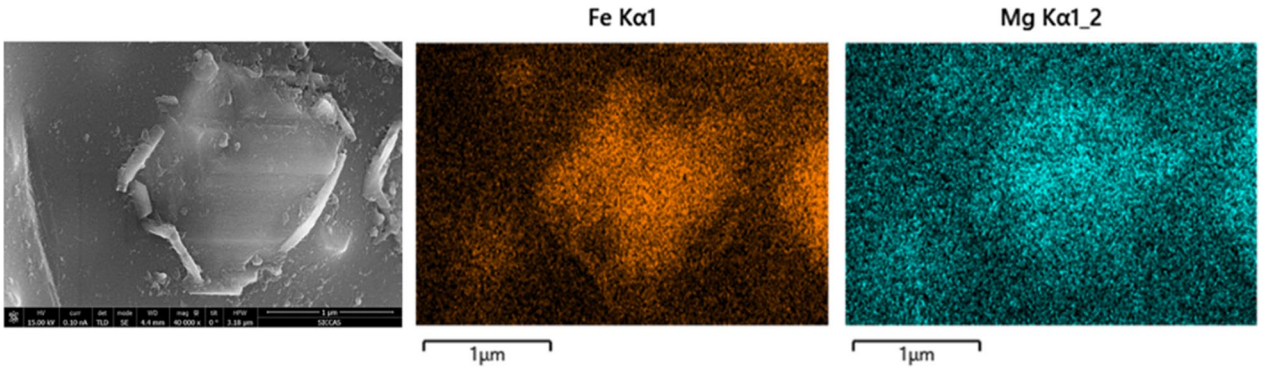

Fig. 11 SEM micromorphology and element distribution at the lamellae in the cross section of NH-1

Table 4 Element contents in different areas of the cross section of NH-1 (wt%)

	C	O	Na	Mg	Al	Si	Cl	K	Ca	Ti	Fe	Mn
P4	13.80	46.44	0.58	–	11.23	24.15	–	2.34	–	–	1.47	–
Figure 10 mapping	27.74	35.44	1.36	0.60	8.29	17.07	1.16	2.42	1.82	0.19	3.67	0.23
Figure 11 mapping	4.99	42.77	0.74	1.98	11.69	19.68	–	2.57	0.67	0.27	13.92	0.73

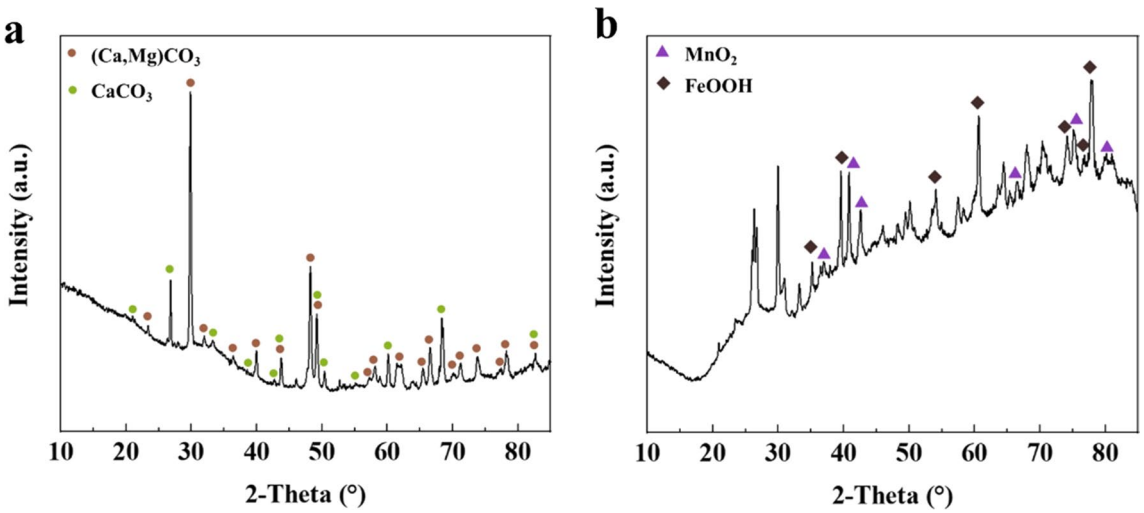

Fig. 12 XRD spectra. **a** NH-1 white shell sediments. **b** Brownish-yellow corrosion regions on the surface of NH-1 after the shedding of the bryozoans

accorded with the valence range of Fe^{2+}. In Fig. 18b, in the S 2p spectrum, the binding energy of 163.9 eV corresponds to S^{2-}.

Infrared spectrum and two-dimensional fluorescence spectrum analysis

Considering the existence of membranous cement on the surface of glazed pottery salvaged from the South China Sea and purple clay teapot from the Yangtze River Estuary, the molecular structure of such membranous cement on the surfaces of NH-1 and CJK-1 was tested by FTIR. As FTIR spectra shown in Fig. 19, the C=O stretching vibration peak of the amide I band was located at 1700-1600 cm^{-1}, the N–H deformation vibration stretching peak of the amide II band was located at 1533 cm^{-1}. Additionally, the peak at 1454 cm^{-1} belonged to the C–H bond, as well as the protein bending vibration peak. The COO– symmetric stretching vibration peak was located at 1404 cm^{-1}. Peaks at 1267 cm^{-1} and 1228 cm^{-1} belonged to C–N stretching vibration and N–H bending

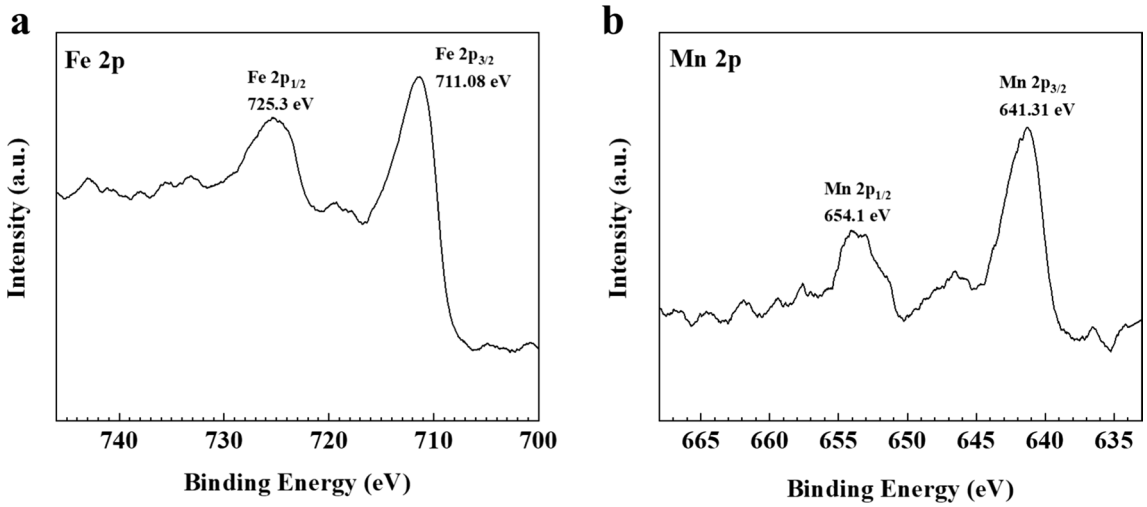

Fig. 13 XPS spectra in the brownish-yellow corrosion regions on the surface of NH-1 after the shedding of the bryozoans. **a** Fe 2p. **b** Mn 2p

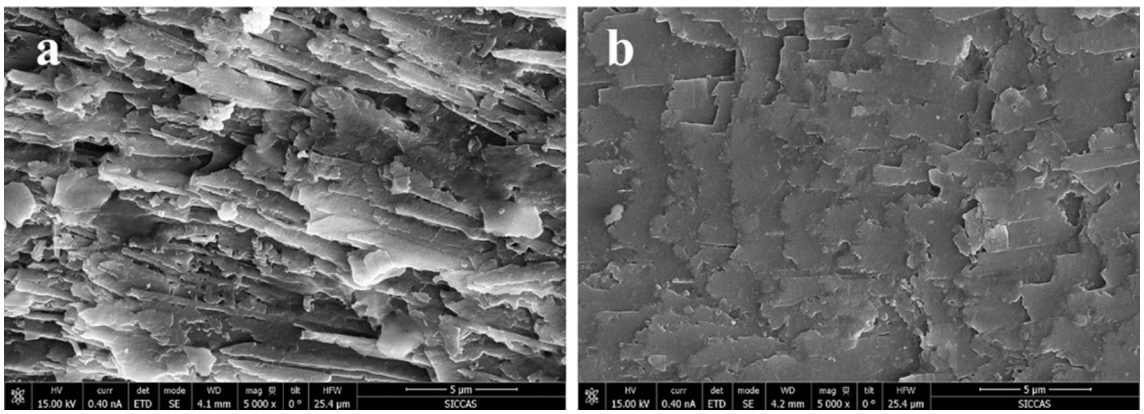

Fig. 14 SEM micromorphology of the oyster surface. **a** Lamellar region. **b** Membranous cement

Table 5 Element contents in different areas of oyster surface (wt%)

	C	O	Na	Mg	Al	Si	Ca	Fe
Figure 14a mapping	8.14	37.45	0.36	0.49	0.63	1.22	50.52	1.18
Figure 14b mapping	11.75	44.09	0.35	0.29	0.07	0.15	42.81	0.49

vibration peaks in the amide III zone. Besides, 1044 cm^{-1} and 800–1000 cm^{-1} were the stretching vibration peaks of carbohydrate C–O, respectively. The above molecular films were protein and carbohydrate cement produced by bryozoans and oysters. Among them, the carbohydrate peak on the black corrosion regions of CJK-1 surface increased significantly, and the characteristic absorption peak of β-pyranoside bond appeared at 890 cm^{-1}. Meanwhile, the C=S stretching vibration absorption band was located at 1200–1020 cm^{-1}, and the membranous cement of the sample was mainly composed of biological proteins and carbohydrate.

Ultraviolet fluorescence was found on the surface of NH-1 and CJK-1. The fluorescence reactions of different samples were measured by PL under excitation wavelength of 220–300 nm and emission wavelength of 250–700 nm. The fluorescence spectra of the samples in Fig. 20 showed the exact position of the emission wavelength and the relative intensity that under excitation wavelength of the fluorescent substance. The excitation

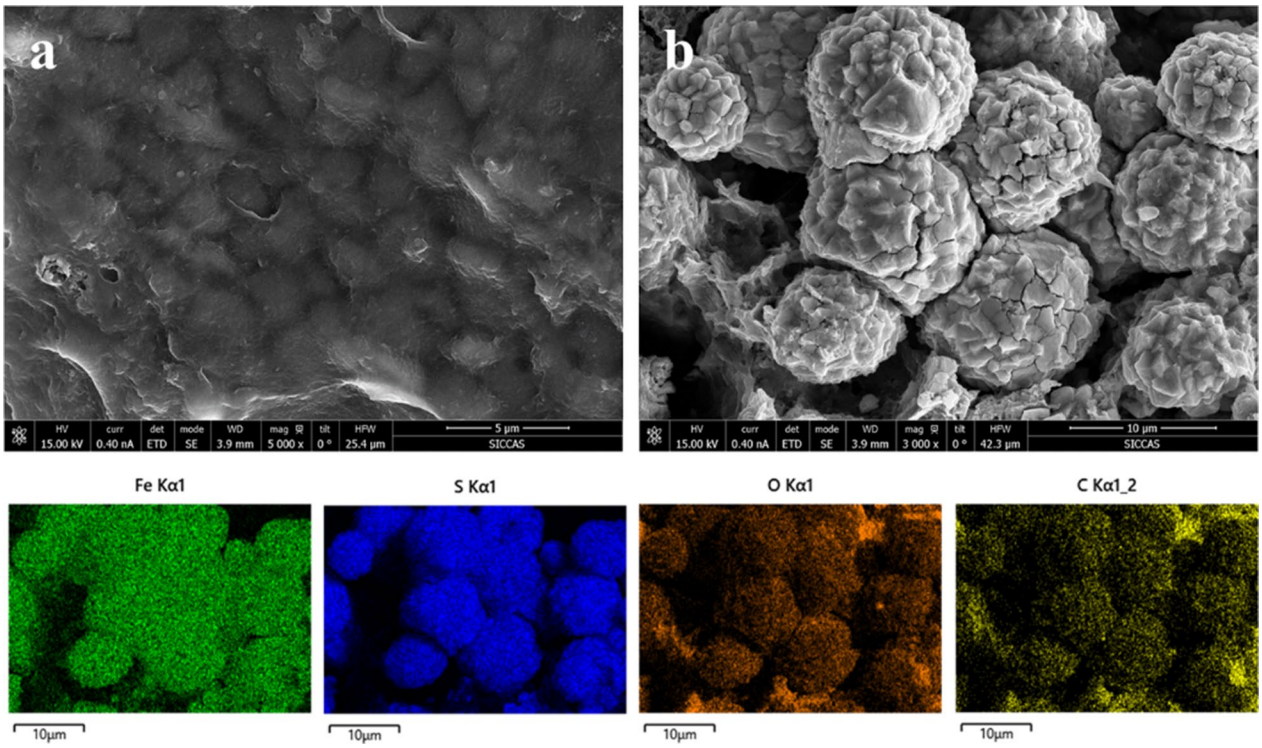

Fig. 15 SEM micromorphology and element distribution of the oyster adhesion surface in contact with the surface of CJK-1. **a** Membranous cement. **b** Flower-cluster substance

bands of brownish-yellow corrosion on the surface of the NH-1 and the black corrosion on surface of CJK-1 were 222 nm and 220 nm respectively, along with the main emission wavelength of 270 nm. Thus, it was confirmed to be the typical fluorescence peaks with proteins (tryptophan-like) as the main products [22]. The emission peaks at 392 nm, 393 nm, 466 and 468 nm were identified to be humus-like fluorophore of natural organic matter in seawater [23].

Previous studies have shown that microorganisms can promote the deposition of Mn in the underwater environment [24, 25]. Manganese-oxidizing bacteria have high Mn enrichment ability and can catalyze the oxidation of Mn(II) ions to Mn(IV) ions and accelerate the deposition of MnO_2 [14]. On top of that, Manganese-oxidizing bacteria accumulate manganese and usually form oxide minerals (as nucleation sites) in the form of biofilms, and those biofilms dominated by manganese oxidizing bacteria can effectively oxidize and precipitate free Fe(II) and Mn(II) ions in seawater into Fe-Mn oxides and hydroxides [26]. It was speculated that the manganese-oxidizing bacteria on the surface of the NH-1 sample were biomineralized using biofilms as a template to generate corrosion products such as iron hydroxide and MnO_2 deposits, and the redox reaction in seawater further converted iron hydroxide into FeOOH [21, 27].

The generation of FeS_2 and FeS on the corroded surface of CJK-1 samples was inferred to be related to the

Table 6 Element contents in different regions of oyster adhesion surface in contact with the surface of CJK-1 (Fig. 15a, b) and of CJK-1 surface in contact with oysters (Fig. 16a–c) (wt%)

	C	O	Na	Mg	Al	Si	Cl	K	Ca	Fe	S
Figure 15a mapping	17.01	32.47	0.52	1.87	0.86	0.87	0.25	–	43.74	1.21	1.20
Figure 15b mapping	14.74	12.04	0.12	0.29	0.34	0.65	–	–	4.00	39.23	28.59
Figure 16a mapping	25.02	19.73	0.30	0.74	2.35	4.91	–	0.52	9.12	22.38	14.93
Figure 16b mapping	5.01	44.14	0.27	0.53	15.65	27.78	–	2.05	–	4.58	–
Figure 16c mapping	18.09	41.41	0.66	1.41	1.13	1.82	0.42	–	33.01	1.40	0.66

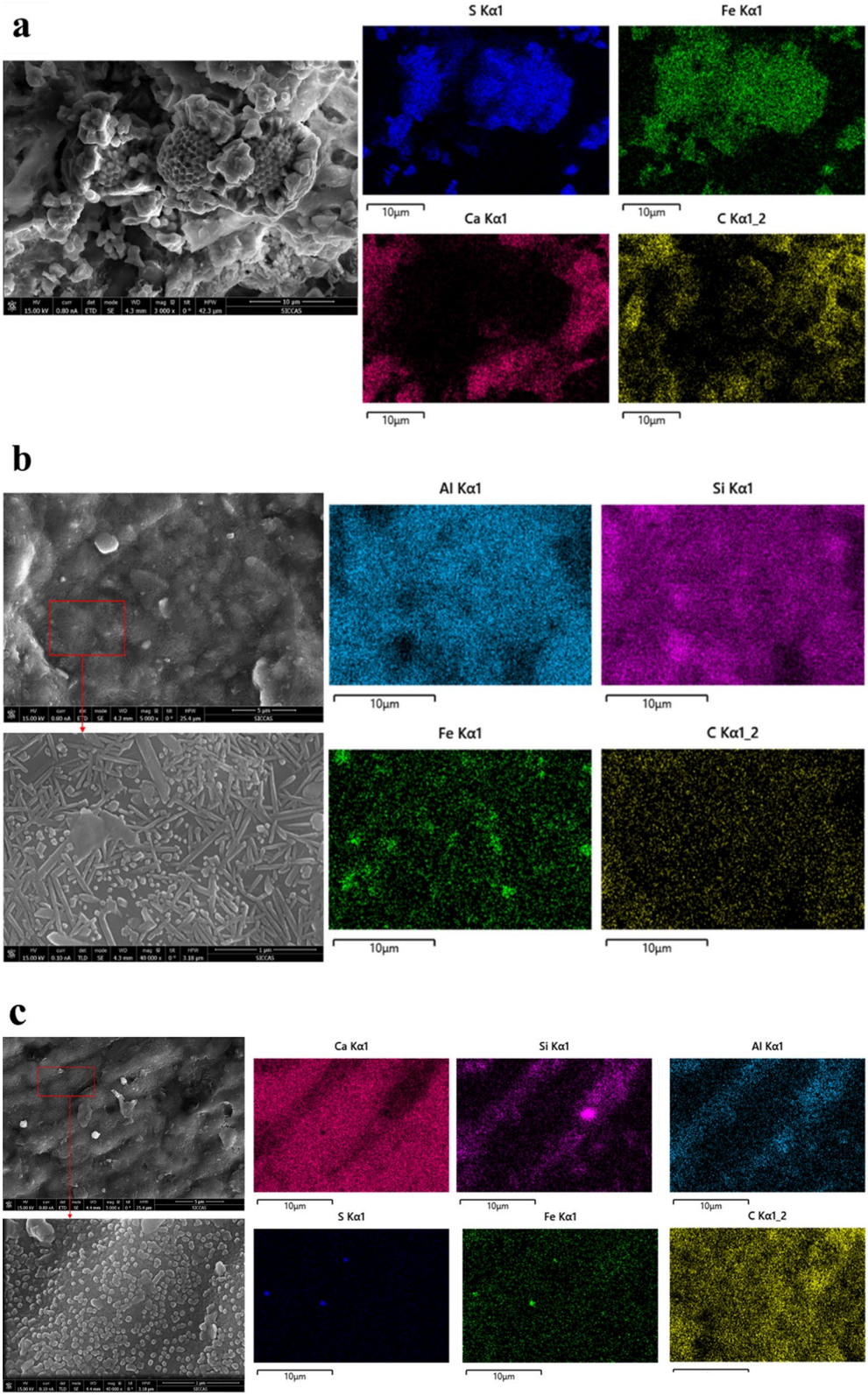

Fig. 16 SEM microscopic morphologies and their element distributions on the surface of CJK-1 in contact with oysters. **a** Flower-cluster substance. **b** Acicular and spherical morphologies

activities of sulfate-reducing bacteria and dissimilating metal-reducing bacteria in the underwater environment of the Yangtze River Estuary [28]. Specifically, sulfate-reducing bacteria can form corrosive biofilms, which corrode attached objects [29–31]. In the anaerobic environment at the bottom of the biofilm, sulfate-reducing bacteria use SO_4^{2-} ions in seawater as terminal electron acceptors in the sulfate reduction reaction, which produces a large number of metabolites H_2S [32]. Dissimilating metal-reducing bacteria use Fe(III) in the insoluble trivalent iron oxide in CJK-1 matrix as the electron acceptor for respiration, and reduce dissolved iron oxide to produce highly active ferrous Fe(II) ions. Fe(III) ions reduction and sulfate reduction always occur simultaneously. Under alkaline seawater conditions, the dissimilated metal-reducing bacteria rely on the active symbiosis or even reciprocal respiration of sulfate-reducing bacteria [33]. Besides, H_2S reacts with Fe(II) ions to form a corresponding FeS thin layer on the cell surface of sulfate-reducing bacteria (as a nucleation site), and the precipitation of FeS thin layer will promote the reaction with H_2S released by bacteria and promote the formation

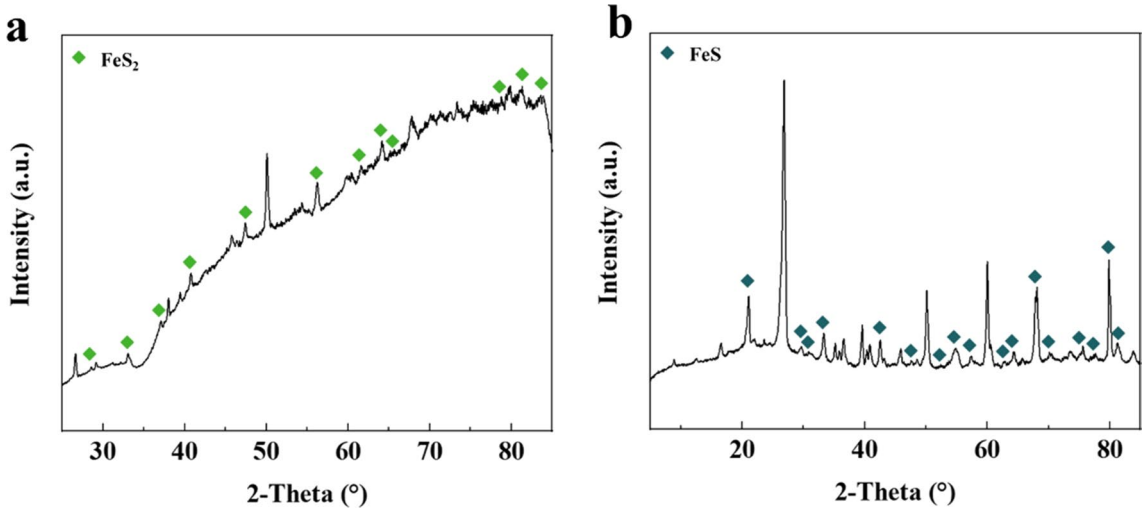

Fig. 17 XRD spectra of different black corrosion regions on the surface of CJK-1 after oysters shedding

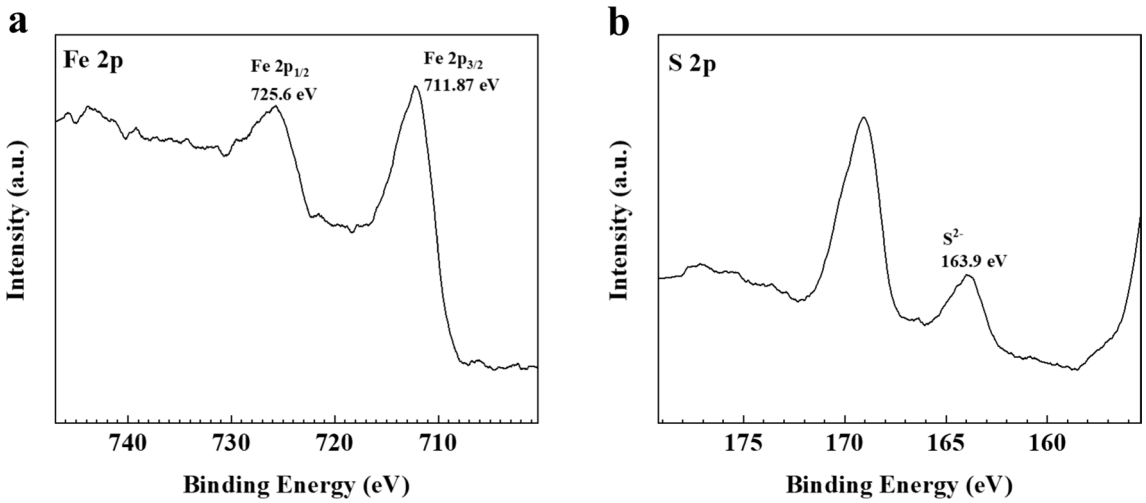

Fig. 18 XPS spectra in black corrosion regions on the surface of CJK-1. **a** Fe 2p. **b** S 2p

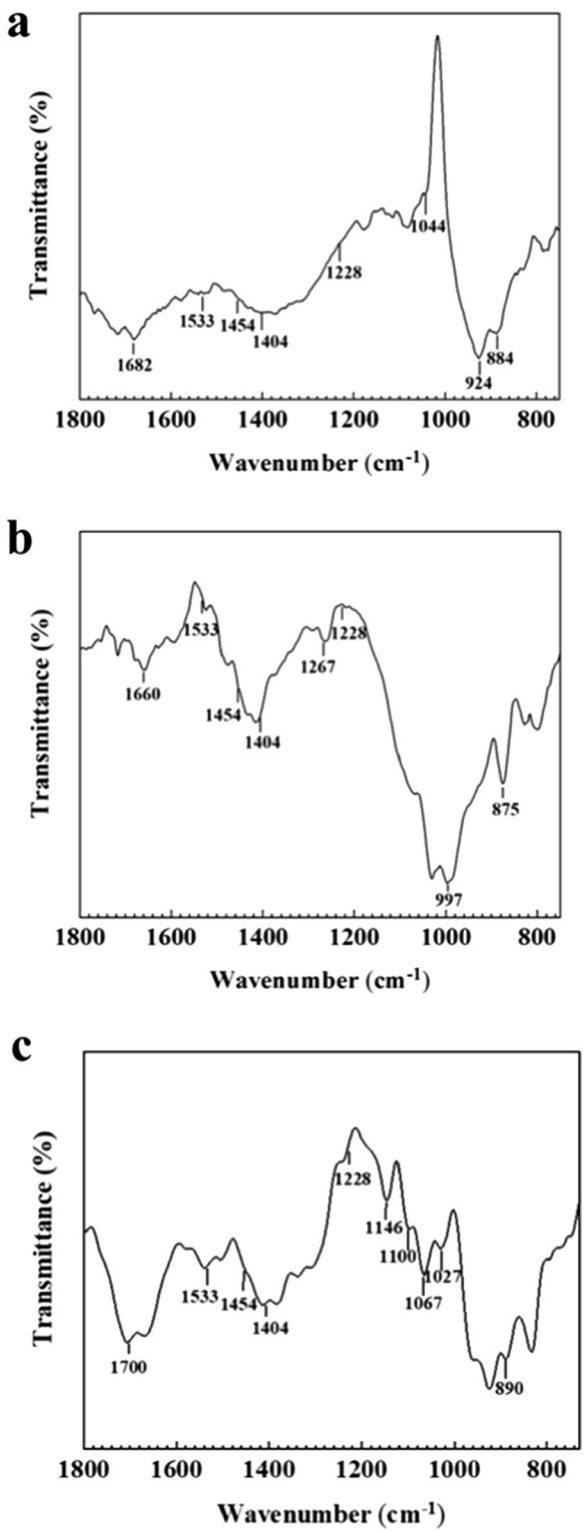

Fig. 19 FTIR spectra. **a** Brownish-yellow corrosion region on the surface of NH-1. **b**, **c** Matrix and black corrosion region on the surface of CJK-1

of FeS_2 [34–38]. It was speculated that the sulfate-reducing bacteria on the surface of CJK-1 sample utilized the corrosive biofilm as a template for biomineralization and produce corrosion metabolites such as FeS_2 and FeS on the bacterial surface.

Corrosion analysis

There were Na and Cl salts on the surface of the glazed pottery sample from the South China Sea, biofilms on the surface and interior of the matrix, and corrosion products such as FeOOH and MnO_2 in the corrosion pits of the cross section. By contrast, the surface of the purple clay teapot fragment from the Yangtze Estuary II shipwreck was covered with biofilm, along with flower-cluster black corrosion products FeS_2 and FeS. Considering the rich microbial environment in the ocean where the pottery relics were located, the corrosion changes on the surface of the pottery samples were speculated to mainly be subject to microbial corrosion, including adhesion of underwater macroscopic organisms, microbial accelerated corrosion (manganese-oxidizing bacteria or dissimilatory metal-reducing bacteria, sulfate-reducing bacteria) and biofilm mineralization.

The organic matters produced by bryozoans, shellfishes and other underwater organisms from the South China Sea and the Yangtze River Estuary adhered to the surface of the pottery samples, serving as the nutrient sources of underwater microorganisms. Furthermore, microorganisms secreted exopolysaccharides, proteins and other extracellular polymers so that their cells could be fixed on the surface of pottery samples and form biofilms. Meanwhile, biofilms and the microenvironment generated by microbial activities, the existence of dissolved metal ions, among others, constructed a chemical microreaction environment before mineral deposition, which determined the location of inorganic mineral mutually reinforcing nuclei and mineral functions. The specific biomineralization process includes:

(1) Microenvironmental control of biomineralization. Extracellular polymers such as proteins and polysaccharides produced by microorganisms contained plenty of hydroxyl and carboxyl functional groups and organic chelates, which built a chemical micro-reaction environment before mineral deposition, determining the location of inorganic mineral mutually reinforcing nuclei and mineral functions. This stage is a premise of biomineralization.
(2) Mineral nucleation and growth regulation: under the regulation of the formed organic membrane, microorganisms, their redox enzymes and extracel-

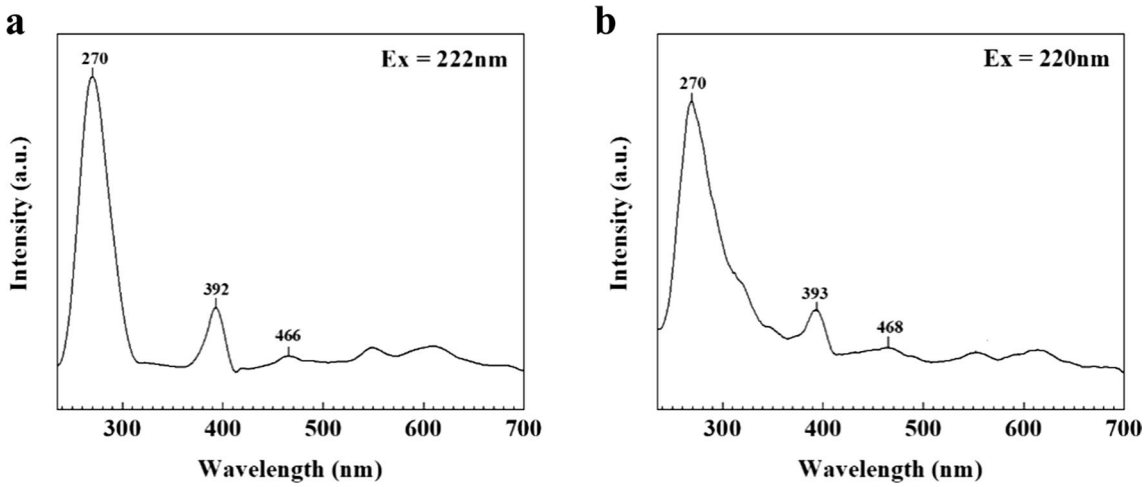

Fig. 20 PL spectra. **a** The brownish-yellow corrosion regions on the surface of NH-1 at excitation of 222 nm and slit of 2 nm. **b** The black corrosion regions on the surface of CJK-1 at excitation of 220 nm and slit of 6 nm

lular macromolecules all acted as electron transporters on the surface of minerals, and free metal ions nucleate at the organic-inorganic interface through physical and chemical effects such as electrostatic attraction, cleavage, hydrogen bonding and even Van Der Waals forces. At the same time, through the slow enrichment of biofilm or organic template at the nucleation site, the local concentration slowly exceeded the solubility product of mineral precipitation, promoting mineral growth.

(3) The inherent physical and chemical actions of the crystals: in the process of complex crystal assembly superstructure, in addition to the organic influencing factors such as biological genes, proteins, polysaccharides and lipids, the inherent physical and chemical actions of mineral crystals also had an impact on the assembly of inorganic minerals, facilitating the emergence of the structure or orderly assembly of biological minerals.

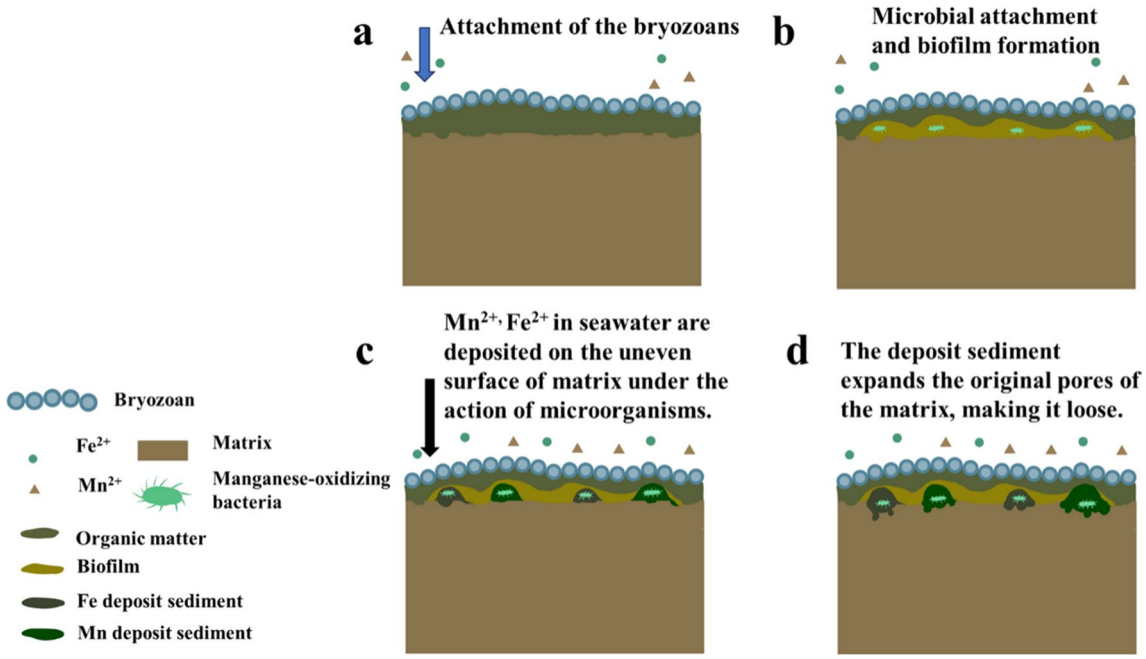

Fig. 21 Corrosion model of NH-1

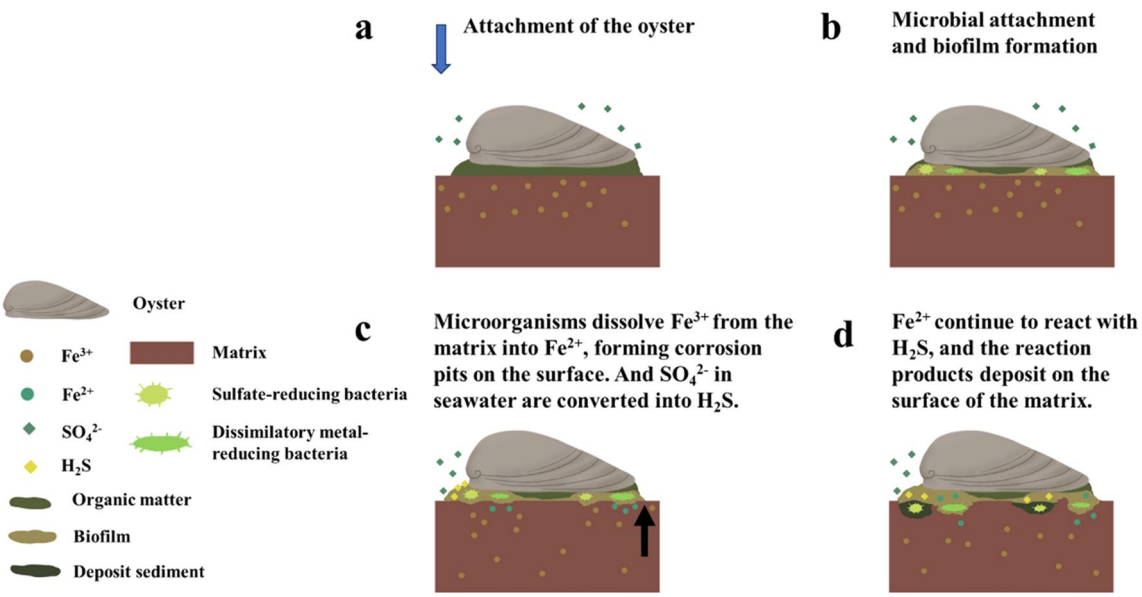

Fig. 22 Corrosion model of CJK-1

The biomineralization process of NH-1 sample is shown in Fig. 21. Underwater organisms such as bryozoans settled on the surface of glazed pottery, and the organic matters secreted by them attracted the attachment of manganese-oxidizing bacteria. Subsequently, the metabolites of manganese oxidizing bacteria formed biofilms on the basis of organic matters. Under the action of manganese oxidizing bacteria, free Mn(II) ions in seawater were oxidized to Mn(IV) ions, forming mineralized sedimentary layer of MnO_2 on the uneven surface of the pottery. At the same time, free Fe ions in seawater also formed iron hydroxide on the uneven surface of cultural relics under the action of manganese-oxidizing bacteria, and FeOOH was generated under the redox action of seawater. The corrosion products gradually accumulated in the unevenness and gaps on the surface of the cultural relics, which loosened their matrix and further deepened the corrosion. The mineralization process of CJK-1 sample is shown in Fig. 22. The organic matters secreted by oysters deposited on the surface of purple clay teapot attracted the attachment of microorganisms such as dissimilatory metal-reducing bacteria and sulfate-reducing bacteria, and the microbial metabolites formed corrosive biofilms based on the organic matters. Under the action of microorganisms, insoluble Fe(III) ions in the matrix of purple clay teapot was reduced to Fe(II) ions by the dissimilatory metal-reducing bacteria, and SO_4^{2-} ions in seawater were converted to H_2S by the sulfate-reducing bacteria. Meanwhile, Fe(II) ions continued to react with H_2S, yielding corrosion mineralized products such as FeS_2 and FeS on the surface of microorganisms, forming corrosion pits on the surface, and further deepening the corrosion of cultural relics.

Conclusion

This study has been able to demonstrate that ceramic pieces are vulnerable to the attachment diseases caused by macroscopic underwater organism like bryozoans and oysters in the underwater preservation environment. This further provides conditions for attachment of underwater sediments and attracts the attachment of microorganisms. According to the morphology, element distribution, infrared functional group test and steady-state fluorescence test of the corrosion area, it is determined that NaCl salt particles were attached to the surface of the pottery relics and corrosion products such as FeOOH, MnO_2 or FeS_2 and FeS were produced. Moreover, the results verify that the pottery samples were mainly corroded by microorganisms, in which the biomineralization of microorganisms on the biofilm aggravated the corrosion of the pottery matrix. Thus, it is speculated that the corrosion difference between the glazed pottery sample from the South China Sea and the purple clay teapot fragment from the Yangtze River Estuary is primarily due to the divergence of the attached manganese-oxidizing bacteria, dissimilatory metal-reducing bacteria and sulfate-reducing bacteria.

Acknowledgements
The authors thank J. Zhao, M. Zhao, K.X. Zhang and H.J. Luo for their support in analysis, Y. Zhai and W.H. Zhou for their help in selecting samples, L. Zhao and Y. Ge for their writing assistance.

Author contributions
The manuscript was written through the contributions of all authors. All authors have given approval to the final version of the manuscript.

Funding
This research was financially supported by the National Natural Science Foundation of Shanghai in China [Grant Numbers: No. 20ZR1422800, No. 23ZR1421000].

Availability of data and materials
Data will be made available on request.

Declarations

Competing interests
The authors declare no competing interests.

Received: 19 October 2023 Accepted: 2 December 2023
Published online: 11 December 2023

References

1. Fernández-Montblanc T, Quinn R, Izquierdo A, Bethencourt M. Evolution of a shallow water wave-dominated shipwreck site: Fougueux (1805), Gulf of Cadiz. Geoarchaeology. 2016;31(6):487–505. https://doi.org/10.1002/gea.21565.
2. Gonzalez-Duarte MM, Fernandez-Montblanc T, Bethencourt M, Izquierdo A. Effects of substrata and environmental conditions on ecological succession on historic shipwrecks. Estuar Coast Shelf Sci. 2018;200:301–10. https://doi.org/10.1016/j.ecss.2017.11.014.
3. Ricca M, Cámara B, Fort R, Álvarez De Buergo M, Randazzo L, Petriaggi BD, La Russa MF. Definition of analytical cleaning procedures for archaeological pottery from underwater environments: the case study of samples from Baia (Naples, South Italy). Mater Des. 2021;197: 109278. https://doi.org/10.1016/j.matdes.2020.109278.
4. Li PN. The trade patterns of the South China Sea during the song period. Asian Archaeol. 2020;3:83–93. https://doi.org/10.1007/s41826-020-00029-z.
5. Yang J, Lan T, Zhang XG, et al. Protomelission is an early dasyclad alga and not a Cambrian bryozoan. Nature. 2023;615:468–71. https://doi.org/10.1038/s41586-023-05775-5.
6. Dobretsov S, Rittschof D. Omics techniques used in marine biofouling studies. Int J Mol Sci. 2023;24(13):10518. https://doi.org/10.3390/ijms241310518.
7. Yan WQ. Overall effluent of the Yangtze Estuary II shipwreck. Grand Garden Sci. 2023;1:70–1. https://doi.org/10.3969/j.issn.1003-1871.2023.01.027. (**in Chinese**).
8. Hang J. Archaeology and preservation of cultural relics of Yangtze Estuary II shipwreck launched, initiating the non-contact overall relocation technique of cultural relics using arched beams. Navigation. 2022;2:4–5 (**in Chinese**).
9. Dong YQ, Song GL, Zheng DJ. Naturally effective inhibition of microbial corrosion by bacterium-alga symbiosis on 304 stainless steel. J Clean Prod. 2022;356: 131823. https://doi.org/10.1016/j.jclepro.2022.131823.
10. Aloise P, Ricca M, La Russa MF, Ruffolo SA, Belfiore CM, Padeletti G, Crisci GM. Diagnostic analysis of stone materials from underwater excavations: the case study of the roman archaeological site of Baia (Naples, Italy). Appl Phys A-Mater Sci Process. 2014;114(3):655–62. https://doi.org/10.1007/s00339-013-7890-1.
11. Ricci S, Sanfilippo R, Basso D, Perasso CS, Antonelli F, Rosso A. Benthic community formation processes of the antikythera shipwreck statues preserved in the National Archaeological Museum of Athens (Greece). J Marit Archaeol. 2019;14(1):81–106. https://doi.org/10.1007/s11457-018-9205-3.
12. Ricca M, La Russa MF. Challenges for the protection of underwater cultural heritage (UCH), from waterlogged and weathered stone materials to conservation strategies: an overview. Heritage. 2020;3(2):402–11. https://doi.org/10.3390/heritage3020024.
13. Antoniadou C, Voultsiadou E, Chintiroglou C. Benthic colonization and succession on temperate sublittoral rocky cliffs. J Exp Mar Biol Ecol. 2010;382(2):145–53. https://doi.org/10.1016/j.jembe.2009.11.004.
14. Jia R, Unsal T, Xu DK, Lekbach Y, Gu TY. Microbiologically influenced corrosion and current mitigation strategies: a state of the art review. Int Biodeterior Biodegrad. 2019;137:42–58. https://doi.org/10.1016/j.ibiod.2018.11.007.
15. Dobretsov S, Qian PY. Facilitation and inhibition of larval attachment of the bryozoan *Bugula neritina* in association with mono-species and multi-species biofilms. J Exp Mar Biol Ecol. 2006;333(2):263–74. https://doi.org/10.1016/j.jembe.2006.01.019.
16. Yu XJ, Yan Y, Gu JD. Attachment of the biofouling bryozoan *Bugula neritina* larvae affected by inorganic and organic chemical cues. Int Biodeterior Biodegrad. 2007;60(2):81–9. https://doi.org/10.1016/j.ibiod.2006.12.003.
17. San NO, Nazir H, Donmez G. Microbiologically influenced corrosion failure analysis of nickel-copper alloy coatings by *Aeromonas salmonicida* and *Delftia acidovorans* bacterium isolated from pipe system. Eng Fail Anal. 2012;25:63–70. https://doi.org/10.1016/j.engfailanal.2012.04.007.
18. Procópio L. Microbially induced corrosion impacts on the oil industry. Arch Microbiol. 2022;204(2):138. https://doi.org/10.1007/s00203-022-02755-7.
19. Dong YQ, Song GL, Xu YQ, Zheng DJ. Bio-inhibitive effect of an algal symbiotic bacterium on corrosion of magnesium in marine environment. J Magnes Alloy. 2023. https://doi.org/10.1016/j.jma.2022.12.008.
20. Wang YR, Zhu TQ, Yang GC, Tan X, Ye DY, Chen HT. The method to soften the concretions of ceramics in the Nanhai I Shipwreck of China Southern Song Dynasty (1127–1279AD). Herit Sci. 2018;6:4. https://doi.org/10.1186/s40494-018-0168-3.
21. Du JN, Luo WG, Li NS, Wang CS. Characterization of the micro-contaminants from the inner-body of Kraak porcelain excavated from the Nan'ao I shipwreck, the South China Sea. Herit Sci. 2019;7(1):85. https://doi.org/10.1186/s40494-019-0328-0.
22. Guo WD, Xu J, Wang JP, Wen YR, Zhuo JF, Yan YC. Characterization of dissolved organic matter in urban sewage using excitation emission matrix fluorescence spectroscopy and parallel factor analysis. J Environ Sci. 2010;22(11):1728–34. https://doi.org/10.1016/S1001-0742(09)60312-0.
23. Trubetskaya OE, Richard C, Trubetskoj OA. High amounts of free aromatic amino acids in the protein-like fluorescence of water-dissolved organic matter. Environ Chem Lett. 2016;14(4):495–500. https://doi.org/10.1007/s10311-016-0556-4.
24. Webb SM, Dick GJ, Bargar JR, et al. Evidence for the presence of Mn(III) intermediates in the bacterial oxidation of Mn(II). PNAS. 2005;102(15):5558–63. https://doi.org/10.1073/pnas.0409119102.
25. Jiang XD, Sun XM, Guan Y. Biogenic mineralization in the ferromanganese nodules and crusts from the South China Sea. J Asian Earth Sci. 2019;171:46–59. https://doi.org/10.1016/j.jseaes.2017.07.050.
26. Jiang XD, Sun XM, Guan Y, Gong JL, Lu Y, Lu RF, Wang C. Biomineralisation of the ferromanganese crusts in the Western Pacific Ocean. J Asian Earth Sci. 2017;136:58–67. https://doi.org/10.1016/j.jseaes.2017.01.025.
27. Ding R, Li WD, Yang ZL, Xu CS, Lu XK. Degradation mechanism of a sauce-glazed ware of the Song Dynasty salvaged out of the water at Dalian Island Wharf: part I—the effect of the surface-attached composite coagula. Materials. 2023;16(3):1176. https://doi.org/10.3390/ma16031176.
28. Tomczyk-Żak K, Szczesny P, Gromadka R, Zielenkiewicz U. Taxonomic and chemical assessment of exceptionally abundant rock mine biofilm. PeerJ. 2017;5: e3635. https://doi.org/10.7717/peerj.3635.
29. Labrenz M, Druschel GK, Thomsen-Ebert T, Gilbert B, Welch SA, Kemner KM, Logan GA, Summons RE, De Stasio G, Bond PL, Lai B, Kelly SD, Banfield JF. Formation of sphalerite (ZnS) deposits in natural biofilms of sulfate-reducing bacteria. Science. 2000;290(5479):1744–7. https://doi.org/10.1126/science.290.5497.1744.
30. Xu D, Wen J, Fu W, Gu T, Raad I. D-Amino acids for the enhancement of a binary biocide cocktail consisting of THPS and EDDS against an SRB biofilm. World J Microbiol Biotechnol. 2012;28(4):1641–6. https://doi.org/10.1007/s11274-011-0970-5.
31. Migaszewski ZM, Gałuszka A. The origin of pyrite mineralization: implications for late Cambrian geology of the Holy Cross mountains (south-central Poland). Sediment Geol. 2019;390:45–61. https://doi.org/10.1016/j.sedgeo.2019.07.004.

32. Liu QY, Li P, Jin ZJ, Liang XP, Zhu DY, Wu XQ, Meng QQ, Liu JY, Fu Q, Zhao JH. Preservation of organic matter in shale linked to bacterial sulfate reduction (BSR) and volcanic activity under marine and lacustrine depositional environments. Mar Pet Geol. 2021;127: 104950. https://doi.org/10.1016/j.marpetgeo.2021.104950.
33. Flynn TM, O'Loughlin EJ, Mishra B, DiChristina TJ, Kemner KM. Sulfur-mediated electron shuttling during bacterial iron reduction. Science. 2014;344(6187):1039–42. https://doi.org/10.1126/science.1252066.
34. Berner RA. Sedimentary pyrite formation: an update. Geochim Cosmochim Acta. 1984;48(4):605–15. https://doi.org/10.1016/0016-7037(84)90089-9.
35. Donald R, Southam G. Low temperature anaerobic bacterial diagenesis of ferrous monosulfide to pyrite. Geochim Cosmochim Acta. 1999;63(13–14):2019–23. https://doi.org/10.1016/S0016-7037(99)00140-4.
36. MacLean LCW, Pray TJ, Onstott TC, Brodie EL, Hazen TC, Southam G. Mineralogical, chemical and biological characterization of an anaerobic biofilm collected from a borehole in a deep gold mine in South Africa. Geomicrobiol J. 2007;24(6):491–504. https://doi.org/10.1080/01490450701572416.
37. Secco M, Maritan L, Mazzoli C, Lampronti GI, Zorzi F, Nodari L, Russo U, Mattioli SP. Alteration processes of pottery in lagoon-like environments. Archaeometry. 2011;53:809–29. https://doi.org/10.1111/j.1475-4754.2010.00571.x.
38. Ferri TZ, Roncevic S, Vrkljan GL, Konestra A. Post-depositional alterations of terrestrial and marine finds of roman ceramics from Crikvenica production centre (NE Adriatic, Croatia)—a contribution towards chemometric classification. J Cult Herit. 2020;43:12–25. https://doi.org/10.1016/j.culher.2019.10.005.

Publisher's Note